

## Direct Mapping of the Electric Permittivity of Heterogeneous Non-Planar Thin Films at Gigahertz Frequencies by Scanning Microwave Microscopy

Received 00th January 20xx,  
Accepted 00th January 20xx

DOI: 10.1039/x0xx00000x

[www.rsc.org/](http://www.rsc.org/)

Maria Chiara Biagi<sup>a</sup>, Giorgio Badino<sup>b</sup>, Rene Fabregas<sup>a,e</sup>, Georg Gramse<sup>c</sup>, Laura Fumagalli<sup>d</sup> and Gabriel Gomila<sup>a,e,†</sup>

We obtained maps of the electric permittivity at ~19 GHz frequencies on non-planar thin film heterogeneous samples by means of combined atomic force-scanning microwave microscopy (AFM-SMM). We show that the electric permittivity maps can be obtained directly from the capacitance images acquired in contact mode, after removing the topographic cross-talk effects. This result demonstrates the possibility to identify the electric permittivity of different materials in a thin film sample irrespectively of their thickness by just direct imaging and processing. We show, in addition, that quantitative maps of the electric permittivity can be obtained with no need of any theoretical calculation or complex quantification procedure when the electric permittivity of one of the materials is known. To achieve these results the use of contact mode imaging is a key factor. For non-contact imaging modes the effects of the local sample thickness and of the imaging distance makes the interpretation of the capacitance images in terms of the electric permittivity properties of the materials much more complex. Present results represent a substantial contribution to the field of nanoscale microwave dielectric characterization of thin film materials with important implications for the characterization of novel 3D electronic devices and 3D nanomaterials.

### Introduction

Near Field Scanning Microwave Microscopes (SMM) emerged in 1972<sup>1</sup> by the need to provide local maps of the electric permittivity properties of heterogeneous materials in a non-destructive way and with micrometric spatial resolution. Fundamentally, a microwave microscope consists of a near-field probe, which can be scanned over the sample, and which is connected to a microwave source/measurement system. When the probe is held close or in contact to the surface of the sample, the sample perturbs the evanescent electromagnetic field. By consequence, the system becomes sensitive to the local complex impedance of the probe-sample system, and hence, to its local complex electric permittivity. Micrometric to deep sub-micrometric spatial resolution measurements can be obtained by engineering special measuring probes. First setups employed traditional microwave elements such as microstrips<sup>2</sup>, coaxial waveguides with tapered end<sup>3</sup> or waveguides with aperture<sup>4</sup> as probes. Lately, combined Atomic Force-Scanning Microwave Microscope systems (AFM-SMM)<sup>5,6,7</sup> were able to use

AFM probes (conventional or engineered<sup>8</sup>) as source of the evanescent field. The size of AFM probes can be easily manufactured down to tens of nanometres, enabling a high spatial lateral resolution (see Ref. 9 for a thorough review). Examples of application of the SMM includes the rapid, non-destructive and local detection of the electric permittivity in insulating materials, ferroelectric and new functional materials discovered by combinatorial synthesis,<sup>10,11,12</sup> which are employed in supercapacitors, batteries, non-volatile memories, diodes and photovoltaic cells. This type of SMM applications are expected to contribute also to the field of new nanomaterials for microwave applications (e.g. nano-composite absorbers).<sup>13,14</sup> In addition, SMM has also been applied to the study of complex oxides,<sup>15</sup> graphene,<sup>16,17</sup> carbon nanotubes,<sup>18</sup> doped semiconductors,<sup>19</sup> and superconductors.<sup>20</sup> Furthermore, SMM will contribute to the emerging field of high frequency nanoelectronic devices, where there is the demand of on-wafer measurement systems sensitive to the microwave electromagnetic properties of dielectric materials.<sup>21</sup>

In spite of the large number of successful applications of the SMM, a main challenge still remains, namely, the difficulty in mapping the electric permittivity of heterogeneous samples exhibiting large height variations. Until now, most applications have dealt with either heterogeneous 2D planar samples<sup>6,12,22,23</sup> or with homogeneous 3D samples,<sup>24</sup> but they have not addressed the general situation of 3D heterogeneous systems, yet. The emergence of the new 3D electron device technologies (e.g. 3D transistors FinFET<sup>25</sup> and 3D NAND memories<sup>26</sup>) and of new 3D functional nanomaterials<sup>27,28,29</sup> is

<sup>a</sup> Institut de Bioenginyeria de Catalunya (IBEC), c/ Baldori i Reixac 11-15, 08028, Barcelona, Spain.

<sup>b</sup> Keysight Technologies Austria GmbH, Keysight Lab, Gruberstr. 40, 4020-Linz, Austria.

<sup>c</sup> Johannes Kepler University Linz, Institute for Biophysics, Gruberstr. 40, 4020-Linz, Austria

<sup>d</sup> School of Physics and Astronomy, University of Manchester, Oxford Road, Manchester, M13 9PL, United Kingdom.

<sup>e</sup> Departament d'Enginyeries: Electrònica, Universitat de Barcelona, C/ Martí i Franqués 1, 08028, Barcelona, Spain.

† Corresponding author: [ggomila@ibecbarcelona.eu](mailto:ggomila@ibecbarcelona.eu)

prompting for a resolution of the above mentioned challenge.<sup>30</sup> The major issue posed by non-planar heterogeneous systems is that the measured microwave signal shows contributions due to both changes in the sample topography and changes in the local electric permittivity properties, whose disentanglement is rather complex.<sup>31</sup>

Here, we present a method to disentangle topographic and electric permittivity variations in the particular case of thin film heterogeneous samples with variable thickness. We show that maps of the electric permittivity of the different materials in the sample in the GHz frequency range can be obtained directly from capacitance images acquired with an AFM-SMM system by simple image processing. To achieve this, we show that contact mode intrinsic capacitance images, obtained from conventional AFM-SMM capacitance images by removal of the topographic cross-talk contributions, can be directly related to the local electric permittivity of the materials in the sample, with no effect of the thickness of the different materials. The use of contact mode imaging is key to achieve this result. Indeed, we show that for non-contact imaging modes, such as for instance intermittent contact mode or two pass modes, very often used with AFM-SMM systems, the relation between intrinsic capacitance images and electric permittivity is

more complex and depends on the film thickness and imaging distance, thus making more difficult the derivation of electric permittivity maps.

## Results

The problematics posed by non-planar heterogeneous thin film samples concerning the measurement of its local electric permittivity properties by means of an AFM-SMM system can be understood by considering a thin film sample consisting of micropatterned oxides of different thicknesses. Figure 1a shows a contact mode topographic image of one of such samples. It consists of  $\text{Al}_2\text{O}_3$  square pillars (located to the left of the image by design) and of square  $\text{SiO}_2$  pillars (located on the right of the image), e-beam evaporated and micropatterned on a gold substrate (see Experimental section for microfabrication details). In this sample the pillars have thicknesses  $h_{\text{Al}_2\text{O}_3}=104$  nm and  $h_{\text{SiO}_2}=65$  nm, respectively (see topographic cross-section profile in Fig. 1b). Figure 1c shows a contact mode (calibrated) capacitance image of the sample obtained at  $\sim 19$  GHz with an AFM-SMM set up (see Experimental section for a description of the set-up, and the SMM calibration procedure used to obtain the capacitance images).

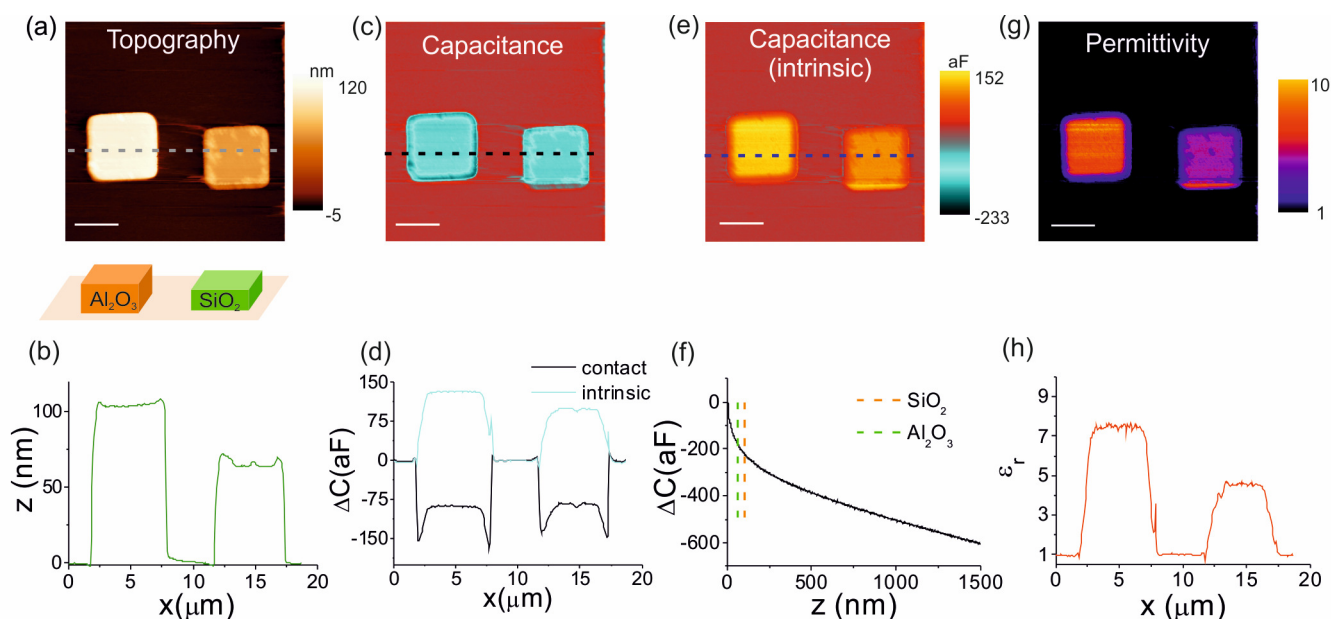


Figure 1. (a) AFM contact mode topography image and (b) corresponding cross-section profile of a thin film sample consisting of micropatterned  $\text{Al}_2\text{O}_3$  (left) and  $\text{SiO}_2$  (right) pillars of different thicknesses on a gold substrate. Pillars thicknesses:  $h_{\text{Al}_2\text{O}_3}=104$  nm and  $h_{\text{SiO}_2}=65$  nm. (c) SMM Contact mode calibrated capacitance image at  $\sim 19$  GHz and (d) corresponding cross-section profile (black line). (e) Intrinsic contact mode capacitance image. The corresponding cross-section profile is shown in (d), blue line. (f) Capacitance approach curve on the bare substrate used, in combination with the topographic image in (a), to reconstruct the intrinsic capacitance image. Note that the curve has been shifted in order to set the capacitance variation at contact with the substrate to the same value obtained from the capacitance image, namely 0 aF. This curve is also used to calibrate the tip radius giving  $R=1173$  nm,  $\theta=10^\circ$  and  $k_{\text{stray}}=0.124$  aF/nm. The vertical dashed lines refer to the thicknesses of the two pillars in the sample. (g) Relative electric permittivity map, and (h) corresponding cross-section profile, obtained from the intrinsic capacitance image in (e) with the use of Eq. (6) and the calibrated tip radius. Scale bar of all images =  $3.8\mu\text{m}$ .

The contact mode capacitance image (Fig. 1c) shows a very similar contrast for the two pillars, just slightly larger for the  $\text{Al}_2\text{O}_3$  pillar than for the  $\text{SiO}_2$  pillar,  $|\delta C_{\text{contact}}^{\text{Al}_2\text{O}_3}| = 87 \pm 1$  aF and  $|\delta C_{\text{contact}}^{\text{SiO}_2}| = 84 \pm 1$  aF,

respectively, see cross-section profile in Fig. 1d (black line). This result is not in line with the expected higher electric permittivity of  $\text{Al}_2\text{O}_3$  with respect to  $\text{SiO}_2$  ( $\epsilon_{r,\text{SiO}_2} < \epsilon_{r,\text{Al}_2\text{O}_3}$ ). This means that the difference in electric permittivities between the two materials can be

compensated by the difference in their respective thicknesses. This problem does not appear if one considers the intrinsic capacitance image shown in Fig. 1e, in which topographic cross-talk effects have been removed (to construct the intrinsic capacitance image we used the capacitance approach curve shown in Fig. 1f and the topographic image in Fig. 1a, see Experimental section). The resulting intrinsic image (Fig. 1e) shows a clear higher contrast for the  $\text{Al}_2\text{O}_3$  pillar ( $|\delta C_{\text{contact.int}}^{\text{Al}_2\text{O}_3}| = 133 \pm 1 \text{ aF}$ ) as compared to the  $\text{SiO}_2$  pillar ( $|\delta C_{\text{contact.int}}^{\text{SiO}_2}| = 99 \pm 1 \text{ aF}$ ), in agreement with the expected larger electric permittivity of  $\text{Al}_2\text{O}_3$  (see also cross-section profile, blue line, in Fig. 1d).

The intrinsic contact mode capacitance images can be used to obtain almost directly quantitative maps of the electric permittivity of the materials. To do so, we use the analytical model proposed in Refs. 32,33 for the tip-sample capacitance on thin film samples (see further discussion on this point in the Discussion section). According to this model, the tip-sample capacitance in a thin film system can be expressed as a sum of apex, cone and stray contributions<sup>32,33,24</sup>:

$$C(z; h, \epsilon_r) = C_{\text{apex}}(z; h, \epsilon_r) + C_{\text{cone}}(z; h, \epsilon_r) + C_{\text{stray}}(z) + C_0 \quad [1]$$

where:

$$C_{\text{apex}}(z; h, \epsilon_r) = 2\pi\epsilon_0 R \ln\left(1 + \frac{R \cdot (1 - \sin(\theta))}{z + h/\epsilon_r}\right); \quad [2]$$

$$C_{\text{cone}}(z; h, \epsilon_r) = \frac{-2\pi\epsilon_0}{\ln[\tan(\frac{\theta}{2})]^2} \left[ \left( z + \frac{h}{\epsilon_r} + R(1 - \sin(\theta)) \right) \ln\left(\frac{H}{z + \frac{h}{\epsilon_r} + R(1 - \sin(\theta))}\right) + R \cdot (1 - \sin(\theta)) + \frac{R \cos^2(\theta)}{\sin(\theta)} \ln\left[z + \frac{h}{\epsilon_r} + R(1 - \sin(\theta))\right] \right]; \quad [3]$$

$$C_{\text{stray}}(z) = -k_{\text{stray}} z; \quad [4]$$

Here,  $C_0$  is a constant value independent from  $z$ ,  $z$  is the tip sample distance,  $R$  is the tip apex radius,  $\theta$  is the cone half angle,  $H$  is the tip cone height and  $k_{\text{stray}}$  is a phenomenological parameter accounting for the long range stray interaction of the cantilever and chip holder with the substrate. Moreover,  $h$  is the thin film thickness and  $\epsilon_r$  its relative electric permittivity. From this model, the intrinsic capacitance contrast at a given position on the sample plane,  $\vec{x} = (x, y)$ , can be expressed as:

$$\delta C_{\text{int}}(\vec{x}) = C(h(\vec{x}) + z_c; \epsilon_r(\vec{x})) - C(h(\vec{x}) + z_c; 1), \quad [5]$$

where  $\epsilon_r(x)$  is the local electric permittivity and  $h(x)$  the local thickness of the sample. Eq. (2), (3), (4) can be substituted into Eq. (1) and this into Eq. (5). As a result the stray component cancels out. Furthermore, under the conditions  $R \gg h(x)$  (thin film), and  $z_c = 0$  (contact mode imaging), one obtains a remarkable simple relation:

$$\delta C_{\text{contact.int}}(\vec{x}) = 2\pi\epsilon_0 R \ln(\epsilon_r(\vec{x})). \quad [6]$$

Equation (6) shows that the contact mode intrinsic capacitance image in a non-planar thin film sample is directly related to the local relative electric permittivity of the sample, with no dependence on the local sample thickness,  $h(x)$ . This result confirms the experimental findings described above. According to Equation 6, quantitative electric permittivity maps can be obtained directly from the intrinsic contact mode capacitance image by just inverting this equation, i.e.,

$$\epsilon_r(\vec{x}) = e^{\frac{\delta C_{\text{contact.int}}(\vec{x})}{2\pi\epsilon_0 R}}, \quad [7]$$

where only the intrinsic capacitance and the tip radius  $R$  need to be known (the tip radius can be determined *in situ*, for instance, by using a capacitance approach curve measured on the metallic substrate as shown elsewhere<sup>24,34,35</sup>). In Fig. 1g we show the electric permittivity image obtained from the intrinsic capacitance image shown in Fig. 1e with the use of Eq. (7) and the calibrated tip radius. The images predict an electric permittivity for the  $\text{Al}_2\text{O}_3$  pillar of  $\epsilon_{r,\text{Al}_2\text{O}_3} = 7.5 \pm 1$  while for the  $\text{SiO}_2$  pillar they predict  $\epsilon_{r,\text{SiO}_2} = 4.5 \pm 0.5$  (the errors have been calculated from error propagation analysis of Eq. (7)). The values obtained for the electric permittivities are in reasonable agreement with the nominal values reported for these materials in the literature, ( $\epsilon_{r,\text{SiO}_2} \sim 4^{36}$ ,  $\epsilon_{r,\text{Al}_2\text{O}_3} \sim 9^{23}$ ).

Similar conclusions are reached by analysing a second sample in which the thicknesses of the two materials are almost identical. A topographic image of this second sample is shown in Fig. 2a, together with a cross-section profile in Fig. 2b. In this case the thicknesses are:  $h_{\text{Al}_2\text{O}_3} = 130 \text{ nm}$  and  $h_{\text{SiO}_2} = 140 \text{ nm}$ . The contact mode SMM capacitance image at  $\sim 19 \text{ GHz}$  (Fig. 2c) shows that the contrast on the centre of the  $\text{Al}_2\text{O}_3$  pillar ( $|\delta C_{\text{contact}}^{\text{Al}_2\text{O}_3}| = 99 \pm 1 \text{ aF}$ ) is smaller than that of the  $\text{SiO}_2$  pillar ( $|\delta C_{\text{contact}}^{\text{SiO}_2}| = 120 \pm 1 \text{ aF}$ ), see cross-section profile (black line) in Fig. 2d. Again the contrasts are not in line with the expected higher electric permittivity of  $\text{Al}_2\text{O}_3$  as compared to that of  $\text{SiO}_2$ . Instead, if we construct the intrinsic capacitance image with the help of the capacitance approach curve on the gold substrate (shown in Fig. 2f) and the topographic image in Fig. 2a, the correct contrast order is obtained. Indeed, from Figure 2e, which shows the obtained intrinsic capacitance image, we observe a higher contrast for the  $\text{Al}_2\text{O}_3$  pillar ( $|\delta C_{\text{contact.int}}^{\text{Al}_2\text{O}_3}| = 134 \pm 1 \text{ aF}$ ) as compared to the  $\text{SiO}_2$  pillar ( $|\delta C_{\text{contact.int}}^{\text{SiO}_2}| = 120 \pm 1 \text{ aF}$ ), see cross-section profile in Fig. 2d (blue line), this time in accordance with the expected higher electric permittivity of  $\text{Al}_2\text{O}_3$ . This result indicates that topographic cross-talk effects may dominate the contact mode SMM capacitance images, even for a sample with just 10 nm difference in thickness like the present one, thus highlighting the importance of these effects. Finally, we construct the electric permittivity image with the help of Eq. (7) and the calibrated tip radius (same as before). The resulting image, together with a cross-section profile, are shown in Figs. 2g and 2h, respectively. The image predicts an electric permittivity for the

$\text{Al}_2\text{O}_3$  pillar of  $\epsilon_{r,\text{Al}_2\text{O}_3}=8\pm 1$  while for the  $\text{SiO}_2$  pillar it predicts  $\epsilon_{r,\text{SiO}_2}=6\pm 1$ .

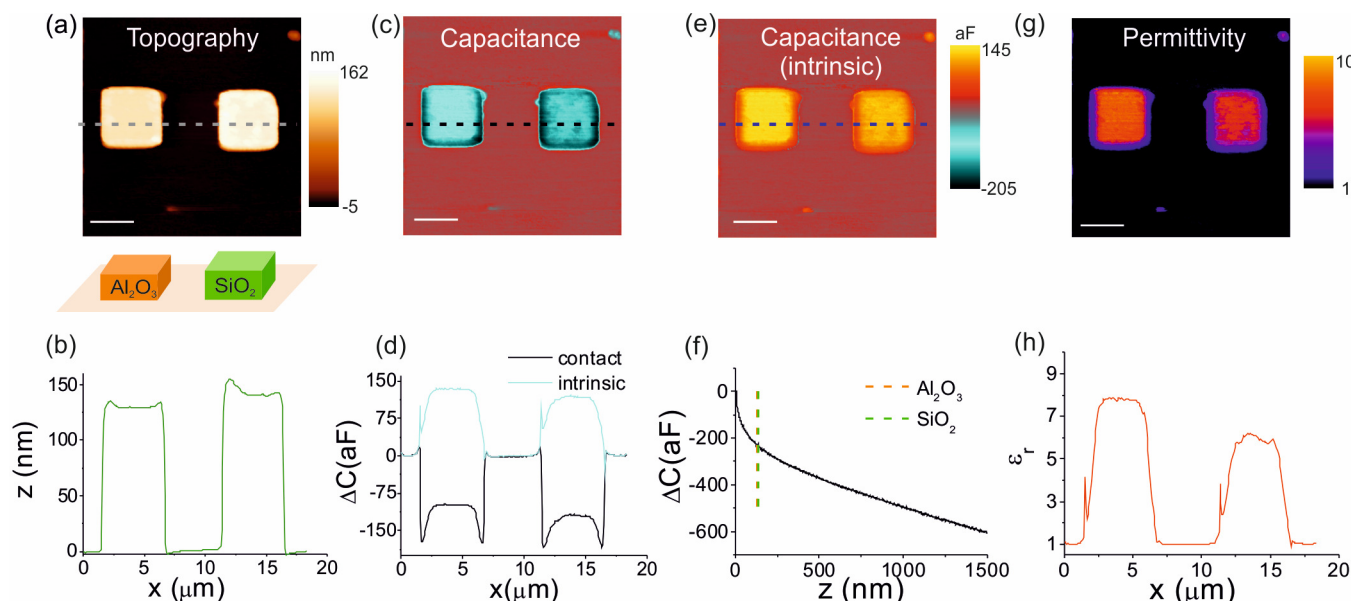


Figure 2. (a) AFM contact mode topography image and (b) corresponding cross-section profile of a thin film sample consisting of micropatterned  $\text{Al}_2\text{O}_3$  (left) and  $\text{SiO}_2$  (right) pillars of different thicknesses on a gold substrate. Pillars thicknesses:  $h_{\text{Al}_2\text{O}_3}=130$  nm and  $h_{\text{SiO}_2}=140$  nm. (c) SMM Contact mode calibrated capacitance image at  $\sim 19$  GHz and (d) corresponding cross-section profile (black line). (e) Intrinsic contact mode capacitance image. The corresponding cross-section profile is shown in (d), blue line. (f) Capacitance approach curve on the bare substrate used, in combination with the topographic image in (a), to construct the intrinsic capacitance image. Note that the curve has been shifted in order to set the capacitance variation at contact with the substrate, to the same value obtained from the capacitance image, namely 0 aF. This curve is also used to calibrate the tip radius giving  $R=1172$  nm,  $\theta=10^\circ$  and  $k_{\text{stray}}=0.137$  aF/nm. The vertical dashed lines, almost indistinguishable, refer to the thicknesses of the two pillars in the sample. (g) Relative electric permittivity map, and (h) corresponding cross-section profile, obtained from the intrinsic capacitance image in (e) with the use of Eq. (6) and the calibrated tip radius. Scale bar of all images =  $3.8\ \mu\text{m}$ .

The value obtained for the  $\text{Al}_2\text{O}_3$  pillar is almost identical to the one obtained for the first sample analysed above. However, for the  $\text{SiO}_2$  pillar we obtained a somewhat larger value. We have verified thoughtfully the quantitative capabilities of the methodology proposed by analysing with it the electric permittivity properties of a micropatterned high quality thermal grown  $\text{SiO}_2$  sample on a highly doped silicon wafer. Results shown in Fig. 3 provide an electric permittivity value of  $\epsilon_{r,\text{SiO}_2}=4.1\pm 0.3$ , in excellent agreement with the nominal value of  $\text{SiO}_2$ . Therefore, we attribute the slightly larger value obtained for the  $\text{SiO}_2$  pillar in the sample of Fig. 2 to a poorer quality of this specific e-beam deposited  $\text{SiO}_2$  (which was deposited several weeks after the sample analyzed in Fig. 1). We remember that the dielectric properties of  $\text{SiO}_2$  are highly sensitive to the quality of the deposited material and to the presence of eventual contaminations, as it has been shown earlier for  $\text{SiO}_2$  deposited by different methods, where in all cases, a larger electric permittivity was reported (Refs.37-39). This result, shows the high sensitivity of the methodology proposed to the actual dielectric properties of the materials.

We have then shown that contact mode SMM capacitance images do not reflect directly the electric permittivity properties of the materials in non-planar heterogeneous thin film samples. Instead,

intrinsic capacitance images, obtained by removing the topographic cross-talk effects, provide direct information on the electric permittivity of the materials and allow deriving in a straightforward way electric permittivity maps of the sample, irrespectively of the thickness of the different materials.

We also note that in the case that the electric permittivity of one of the materials in the sample is known, then one can derive the electric permittivity values of the other materials without even knowing the geometry of the measuring tip. Indeed, from Eq. 6, it is immediate to show that the electric permittivity of two regions of a sample satisfies the relationship

$$\epsilon_r(\vec{x}) = \epsilon_r(\vec{x}_{ref}) \left( \frac{\delta C_{int}(\vec{x})}{\delta C_{int}(\vec{x}_{ref})} \right), \quad [8]$$

which is solely dependent on the ratio of intrinsic capacitance contrasts and on the electric permittivity of the reference material. This result represents a crucial advantage in imaging heterogeneous thin film non-planar samples, since by only knowing the electric permittivity of one material, one can obtain an electric permittivity map directly from the the intrinsic capacitance image by just rescaling the image according to Eq. (8).

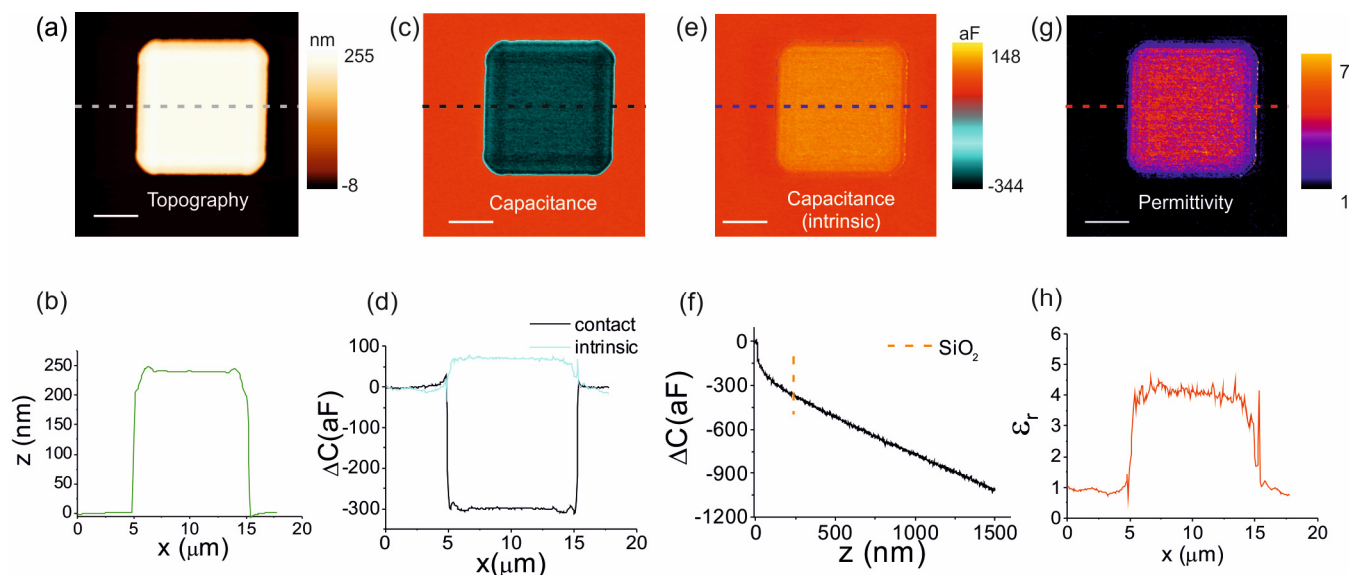


Figure 3. (a) AFM contact mode topography image and (b) corresponding cross-section profile of a thin film sample consisting of micropatterned  $\text{SiO}_2$  pillars of  $h_{\text{SiO}_2}=240$  nm thickness on a highly doped silicon substrate. (c) SMM Contact mode calibrated capacitance image at  $\sim 19$  GHz and (d) corresponding cross-section profile (black line). (e) Intrinsic contact mode capacitance image. The corresponding cross-section profile is shown in (d), blue line. (f) Capacitance approach curve on the bare substrate used, in combination with the topographic image in (a), to construct the intrinsic capacitance image. Note that the curve has been shifted in order to set the capacitance variation at contact with the substrate to the same value obtained from the capacitance image, namely 0 aF. This curve is also used to calibrate the tip radius giving  $R=802$  nm,  $\theta=10^\circ$  and  $k_{\text{stray}}=0.4274$  aF/nm. The vertical dashed line refers to the thicknesses of the pillars in the sample. (g) Relative electric permittivity map, and (h) corresponding cross-section profile, obtained from the intrinsic capacitance image in (e) with the use of Eq. (6) and the calibrated tip radius. Scale bar of all images =  $3.8\mu\text{m}$ .

## Discussion

We have seen that contact mode intrinsic capacitance images obtained with an AFM-SMM system on non-planar thin film heterogeneous samples can be directly interpreted in terms of the electric permittivity of the materials, with no effects associated to the sample thickness. It is important to highlight that this statement holds true as long as the images are obtained in contact mode. To show it, we have obtained SMM capacitance images in intermittent contact mode and analyzed them following the same procedure described above. In Figs. 4a and 4c we show intermittent contact mode SMM capacitance images acquired at  $\sim 19$  GHz on the sample of Fig. 2 ( $h_{\text{Al}_2\text{O}_3}=130$  nm and  $h_{\text{SiO}_2}=140$  nm) at two different oscillation amplitudes, corresponding to mean tip-sample distances  $z_c=30$  nm and  $z_c=90$  nm, respectively. It can be observed from the capacitance images, and from the capacitance cross-section profiles shown in Fig. 4e (black and grey lines for  $z_c=30$  nm and  $z_c=90$  nm, respectively), that the capacitance contrast decreases by increasing the average tip-sample distance, as expected. For the two distances considered, the intermittent contact capacitance contrast is larger for the  $\text{SiO}_2$

pillar ( $|\delta C_{\text{non-contact}}^{\text{SiO}_2}|_{z_c=30\text{nm}} = 55 \pm 2$  aF, ( $|\delta C_{\text{non-contact}}^{\text{SiO}_2}|_{z_c=90\text{nm}} = 39 \pm 3$  aF) as compared to the  $\text{Al}_2\text{O}_3$  pillar ( $|\delta C_{\text{non-contact}}^{\text{Al}_2\text{O}_3}|_{z_c=30\text{nm}} = 48 \pm 2$  aF, ( $|\delta C_{\text{non-contact}}^{\text{Al}_2\text{O}_3}|_{z_c=90\text{nm}} = 34 \pm 3$  aF), again opposite to the expected dielectric response of the materials. Figures 4b and 4d show the corresponding intrinsic capacitance images resulting from the subtraction of the topographic cross-talk contributions. For the smaller tip-sample distance,  $z_c=30$  nm, the intrinsic contrast for the  $\text{Al}_2\text{O}_3$  pillar ( $|\delta C_{\text{non-contact,int}}^{\text{Al}_2\text{O}_3}|_{z_c=30\text{nm}} = 80 \pm 1$  aF) is larger than that of the  $\text{SiO}_2$  pillar ( $|\delta C_{\text{non-contact,int}}^{\text{SiO}_2}|_{z_c=30\text{nm}} = 76 \pm 1$  aF), in line with the expected electric permittivity values. However, for the larger tip-sample distance ( $z_c=90$  nm), the intrinsic capacitance contrasts of both pillars are the same within the experimental error ( $|\delta C_{\text{non-contact,int}}^{\text{Al}_2\text{O}_3}|_{z_c=90\text{nm}} = 44 \pm 2$  aF and  $|\delta C_{\text{non-contact,int}}^{\text{SiO}_2}|_{z_c=90\text{nm}} = 43 \pm 2$  aF). Therefore, while at short tip-sample distances the intrinsic intermittent contact capacitance images still may reflect to some extent the electric permittivity properties of the materials, at larger

distances this is no longer the case, and the interpretation of the images has to be made with caution.

This result can be simply understood by considering the analytical model for the tip-sample capacitance in Eqs. (1)-(4) for the case that the tip-sample distance is different from zero,  $z_c \neq 0$ . One obtains the following expression for the intrinsic capacitance contrast

$$\delta C_{\text{non-contact,int}}(\vec{x}) = 2\pi\epsilon_0 R \ln\left(\frac{z_c + h(\vec{x})}{z_c + \frac{h(\vec{x})}{\epsilon_r(\vec{x})}}\right); \quad [9]$$

i.e., the intrinsic capacitance contrast in non-contact imaging modes, depends not just on the local electric permittivity of the sample, but also on its topography,  $h(x)$ , and on the tip-sample distance at which the image is acquired,  $z_c$ .

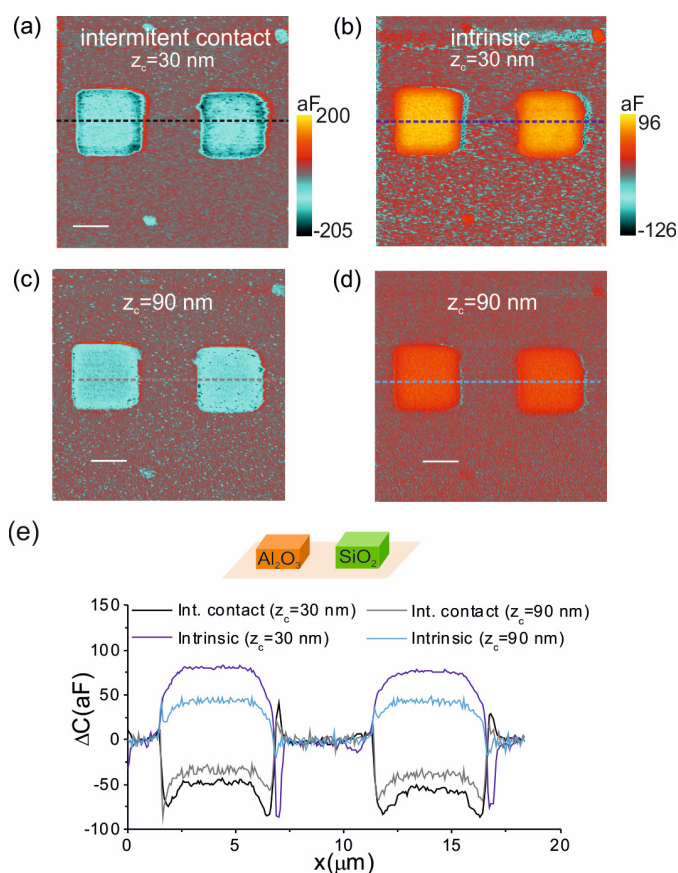


Figure 4. SMM capacitance and intrinsic capacitance images acquired at  $\sim 19$ GHz on the sample shown in Fig. 2 but acquired in intermittent mode at two different oscillation amplitudes: (a)-(b):  $z_c = 30$  nm and (c)-(d)  $z_c = 90$  nm. (e) Cross-section profiles along the lines in the images.

As a consequence, the intrinsic capacitance image does not reflect directly the electric permittivity of the materials in all situations. To illustrate it, in Fig. 5a we plot the intrinsic non-contact capacitance contrast as a function of the imaging distance,  $z_c$ , as predicted by Eq. (9) for the sample analyzed in Fig. 4 (thick green line  $\text{SiO}_2$ :  $h_1 = 140$  nm,  $\epsilon_1 = 6$  and thick orange line  $\text{Al}_2\text{O}_3$ :  $h_2 = 130$  nm,  $\epsilon_2 = 8$ ). The figure shows that for imaging distances larger than  $z_c^* = 189$  nm the order of the intrinsic capacitance contrast of the two pillars would become

reversed in the intrinsic non-contact capacitance image (i.e. even if  $\epsilon_{r,1} < \epsilon_{r,2}$  one would obtain  $\delta C_{\text{non-contact,int},1} > \delta C_{\text{non-contact,int},2}$ ).

Note, also, that at the distance of the measurement reported in Fig. 4d,  $z_c = 90$  nm, (dot-dashed dark blue vertical line in Fig. 5a), the two pillars show an almost identical contrast, as we have obtained experimentally. Instead, at  $z_c = 30$  nm (dot-dashed light blue line in Fig. 5a), the order of the contrasts is not reversed, also as found experimentally (see Fig. 4b). The imaging distance at which the contrast between two regions becomes reversed depends on the relative values of their thicknesses (and on their electric permittivity values). We show it explicitly in Fig. 5a, where we plot also the predictions of the intrinsic capacitance contrasts that would have been obtained for  $\text{Al}_2\text{O}_3$  pillars of heights  $h_{\text{Al}_2\text{O}_3} = 50$  nm (orange dashed line), 100 nm (dot-dashed orange line) and 160 nm (dotted line).

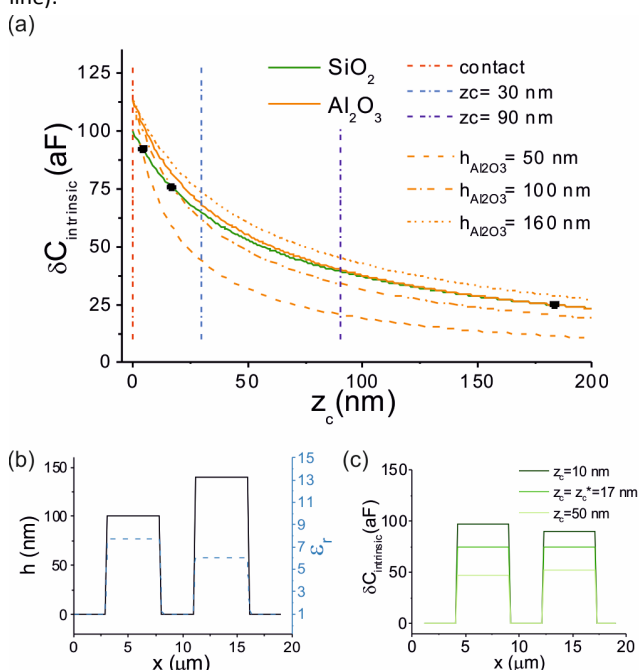


Figure 5. (a) Intrinsic capacitance as function of tip-sample imaging distance for a sample with thin film pillars of  $\text{SiO}_2$  and  $\text{Al}_2\text{O}_3$  calculated according to Eq. (9) (tip radius  $R = 1000$  nm). The thick lines represent  $\text{SiO}_2$  (green) and  $\text{Al}_2\text{O}_3$  (orange) pillars with properties equal to the ones determined for sample in Fig. 2:  $h_{\text{Al}_2\text{O}_3} = 130$  nm,  $\epsilon_{r,\text{Al}_2\text{O}_3} = 8$  and  $h_{\text{SiO}_2} = 140$  nm,  $\epsilon_{r,\text{SiO}_2} = 6$ . The thick line curves intersect at  $z_c^* = 189$  nm, indicating a reverse of the contrast order for distances larger than this. At  $z_c = 90$  nm (dark blue dot-dashed vertical line) the contrasts are almost indistinguishable. Instead at  $z_c = 0$  nm (red dot-dashed vertical line) and  $z_c = 30$  nm (light blue dot-dashed vertical line) the contrasts are not reversed and are ordered according to the electric permittivity of the materials. The dashed, dot-dashed and dotted orange lines represent the predictions of Eq. (8) for the case of different heights of the  $\text{Al}_2\text{O}_3$  pillar:  $h_{\text{Al}_2\text{O}_3} = 50$  nm, 100 nm, 160 nm, respectively. The distances at which reversal occurs (if any) are marked by a black circle, and are in agreement with Eq. (10). (b) Topographic and electric permittivity profiles of a sample used to illustrate the concept of contrast reversal ( $h_{\text{Al}_2\text{O}_3} = 100$  nm,  $\epsilon_{r,\text{Al}_2\text{O}_3} = 8$  and  $h_{\text{SiO}_2} = 140$  nm,  $\epsilon_{r,\text{SiO}_2} = 6$ ). (c) Theoretical non-contact intrinsic capacitance contrasts at three different imaging distances,  $z_c = 10$  nm, 17 nm, 50 nm.

nm and 50 nm, showing that contrast reversal occurs already at  $z_c > z_c^* = 17$  nm.

For the lower pillars the intrinsic contrast reversal would occur already at shorter imaging distances ( $z_c^* = 5$  nm and 17 nm for the  $\text{Al}_2\text{O}_3$  pillars of 50 nm and 100 nm thickness, respectively). Instead, for the taller pillar ( $h_{\text{Al}_2\text{O}_3} = 160$  nm) it would not occur at any imaging distance. The meaning of the contrast reversal is illustrated in Figs. 5b and 5c for the case of a sample with  $h_{\text{Al}_2\text{O}_3} = 100$  nm. It can be shown that, in general, the contrast order reverses with respect to the electric permittivity values for imaging distances larger than a critical distance given by

$$z_c^* = \frac{\frac{h_1 h_2}{\epsilon_{r,1}} - \frac{h_1 h_2}{\epsilon_{r,2}}}{h_2 - h_1 + \frac{h_1}{\epsilon_{r,1}} - \frac{h_2}{\epsilon_{r,2}}} \quad [10]$$

In Fig. 5a, the black circles represent precisely the values predicted by Eq. (10). Finally, we highlight once more, that for contact measurements,  $z_c = 0$  nm, (dot-dashed red line in Fig. 5a) the contrast order is never reversed with respect to the corresponding electric permittivity values, as we have shown before.

We note that even if the extraction of quantitative electric permittivity images from non-contact capacitance images is less direct than for contact images, since it requires the knowledge of the sample topography and of the tip-sample distance, in addition to the tip radius, it is still possible to obtain them if required (e.g. when dealing with biological samples), as we have shown recently,<sup>24</sup> and, also in the past, for low frequency capacitance measurements.<sup>40</sup>

The results derived here are, in principle, valid as long as the analytical model in Eqs.(1)-(4) remains valid. We have discussed in Ref. 33 that the thin film analytical model is valid for thin planar films showing lateral dimensions larger, and thickness smaller, than the tip radius (typically it constitutes an excellent approximation for film thicknesses smaller than half the tip radius), what cover a broad range of situations. When these conditions are not met, then, even the contact mode intrinsic capacitance becomes dependent on both the lateral dimensions of the thin film and its thickness. We show it explicitly in Fig. 6 where we plot the contact intrinsic capacitance numerically calculated (see Experimental section for details) for the case of a sample with  $\text{Al}_2\text{O}_3$  and  $\text{SiO}_2$  pillars of lateral dimensions smaller than the tip radius (here  $R = 1000$  nm). As it can be seen, for sample radii smaller than the tip radius there is a dependence of the contact intrinsic capacitance on the lateral dimensions of the thin film and on its thickness, which prevents using the simple relation in Eq. (6). In this case, one has to resort to numerical simulations to extract and map the electric permittivity values of the sample. Instead, for larger sample diameters, the intrinsic capacitance becomes independent from the lateral dimensions of the thin film and from its thickness, and only depends on the electric permittivity (and tip radius), as shown before. In particular, the dimensions of the samples analyzed here fall within this latter range (vertical green

lines), and hence these samples can be described by the analytical model, as we did above.

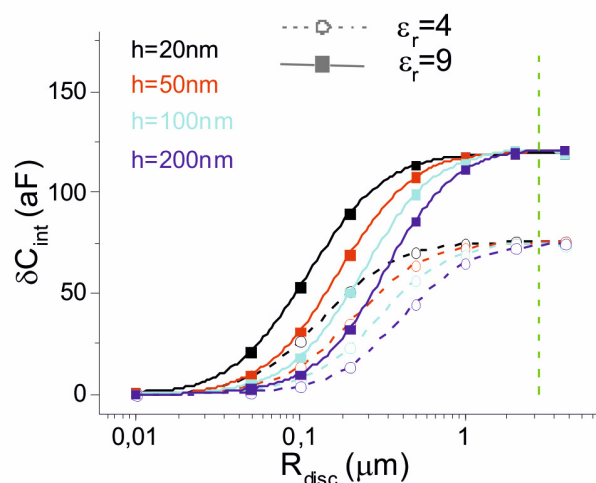


Figure 6. Numerically calculated intrinsic contact capacitance for dielectric discs of different thicknesses,  $h = 20$  nm, 50 nm, 100 nm and 200 nm, as a function of disc radius  $R_{disc}$  and for two different electric permittivities,  $\epsilon_r = 4$  and 9. The tip radius is  $R = 1000$  nm and the half cone angle is  $\theta = 10^\circ$ . For  $R_{disc} \gg R$ , the intrinsic contact capacitance does not depend anymore on the disc radius, therefore it be approximated by Eqs. (1)-(4). The vertical line represent the dimensions of the pillars in the samples analyzed in Fig. 1 and 2 (equivalent  $R_{disc} = 2820$  nm), which fall within the range of validity of the analytical model.

A direct consequence of what discussed above is that when a sample shows some heterogeneities (e.g. a multiphase dielectric thin film) with lateral dimensions smaller than the tip radius, the intrinsic contact capacitance is not longer local, i.e. the intrinsic contact capacitance of at a given position in the sample becomes dependent on the electric permittivity of the surrounding region. We illustrate it in Fig. 7, where we show the intrinsic contact capacitance calculated in the center of a heterogeneity in a multiphase thin dielectric film, consisting of two concentric discs of different thickness and different electric permittivities. When the lateral dimensions the heterogeneity are significantly larger than the tip radius, the numerically calculated intrinsic contact capacitance as a function of the electric permittivity of the heterogeneity depends only on the electric permittivity of the heterogeneity, and it is not affected by the electric permittivity of the surrounding region. In this case, the intrinsic contact capacitance is a local quantity and can be univocally related to the local electric permittivity of the sample according to Eq. (6), following the procedure developed in the present work. However, when the lateral dimensions of the heterogeneity is smaller than the tip radius, this is not longer the case, and the intrinsic contact capacitance becomes non-local, i.e., it depends also on the electric permittivity of the surrounding region. In this case, the intrinsic contact capacitances at a given point in the sample is not univoquely related to the local electric permittivity of the sample. In this case, in order to map the electric permittivity of the thin film one has to resort, not only to numerical calculations, but

also to complex inverse image reconstruction algorithms still not available, and hence lying outside the scope of the present work.

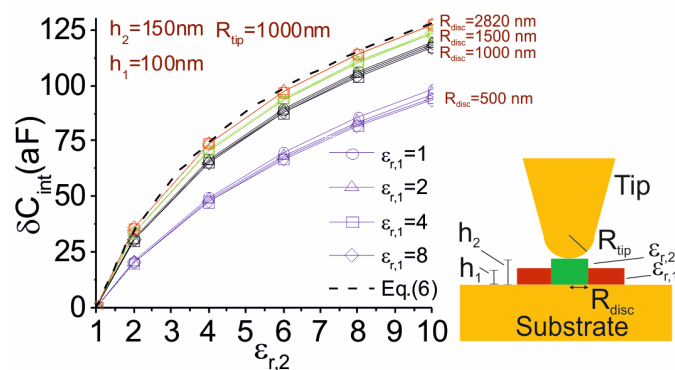


Figure 7. (Symbols) Numerically calculated intrinsic contact capacitance for a multiphase thin film consisting of two concentric dielectric discs (schematically represented on the right of the plot), as a function of the electric permittivity of the central disc,  $\epsilon_{r,2}$ , for different radii of the central disc,  $R_{disc}=500, 1000, 1500$  and  $2820$  nm, and for four different relative electric permittivities of the surrounding disc,  $\epsilon_{r,1} = 1, 2, 4$  and  $8$ . The radius of the external disc is  $R_{ext} = 2820$  nm. The tip radius is  $R_{tip}=1000$  nm and the half cone angle is  $\theta=10^\circ$  (the lines are guides to the eyes). (Dashed line) Theoretical prediction of the intrinsic contact capacitance according to Eq. (6). For  $R_{disc} \gg R_{tip}$ , the intrinsic contact capacitance does not depend neither on the radius of the heterogeneity (central disc) nor on the electric permittivity of the surrounding matrix, and it can be well approximated by Eq. (6). Instead, for  $R_{disc} < R_{tip}$  the intrinsic contact capacitance becomes non-local.

Another situation of interest refers to the case of multistacked thin dielectric films. In this case it can be shown that, under the conditions of validity of Eq. (6) discussed above, the intrinsic contact capacitance is sensitive only to the effective electric permittivity of the whole multistacked thin film,  $\epsilon_{r,eff}$ . By means of numerical calculations it can be shown that also for an AFM-SMM measuring system the effective electric permittivity is given by the well-known relationship (written here for a two stacked thin film)

$$\epsilon_{r,eff} = \frac{h_1 + h_2}{\frac{h_1}{\epsilon_{r,1}} + \frac{h_2}{\epsilon_{r,2}}} \quad [11]$$

where  $h_1$  and  $h_2$ , and  $\epsilon_{r,1}$  and  $\epsilon_{r,2}$ , are the corresponding thin film thicknesses and electric permittivities of the two stacked thin films, respectively, and where  $h_T=h_1+h_2$  is the total thickness of the thin film. We show it explicitly in Fig. 8, where we plot the effective permittivity of a two-stacked thin dielectric film numerically calculated for an AFM-SMM probe-thin film system (red symbols) as a function of the thickness of one of the stacked components for two total thicknesses of the film,  $h_T=50$  nm and  $100$  nm. The calculated results nicely agree with the analytical expression in Eq. (11) (black dashed lines). We note that when the conditions for the validity of Eq. (6) are not met, then Eq. (11) does not remain valid and the effective electric permittivity has to be re-calculated by means of numerical calculations.

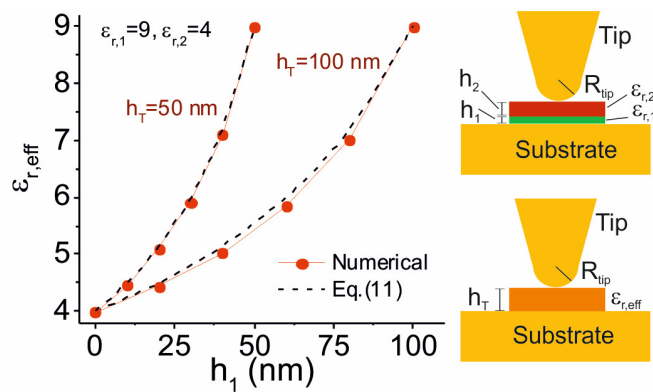


Figure 8. (Symbols) Numerically calculated effective electric permittivity for a two stacked thin dielectric film (schematically represented on the upper right of the plot) for two different total thicknesses  $h_T=50$  nm and  $100$  nm, as a function of the thickness of the bottom stacked thin film,  $h_1$  (the lines are guides to the eyes). The electric permittivities of the stacked films are  $\epsilon_{r,1}=4$  and  $\epsilon_{r,2}=9$  and its lateral dimension is  $R_{disc} = 2820$  nm. The tip radius is  $R_{tip}=1000$  nm and the half cone angle is  $\theta=10^\circ$ . (Dashed black line) Analytical expression for the effective electric permittivity given by Eq. (11) corresponding to an equivalent homogeneous thin film (schematically represented on the lower right of the plot). The numerically calculated results nicely agree with Eq. (11) since the conditions  $R_{disc} \gg R_{tip} \gg h_T$  are met.

To end up, we would like to stress that the problematics of disentangling topographic from electric permittivity contributions in AFM-SMM capacitance images can not be solved by other approaches proposed to date, which involve the use of alternative imaging modes, such as constant height imaging,<sup>41</sup> the use of special tip configurations, such as shielded probes<sup>6,8</sup> and open ended coaxial probes,<sup>3</sup> or the use of specific post-processing algorithms, such as time domain.<sup>42</sup> For instance, constant height imaging by definition contains no topographic cross-talk effects, since the probe-substrate distance is not varied. However, in non-planar samples it provides optimal signal to noise ratio only on the tallest parts of the sample, i.e. the ones closest to the tip, losing accuracy when thickness variations in the hundred of nanometer are present in the sample. Shielded probes or open ended coaxial probes, on their side, limit the non-local interactions with the samples, i.e. the stray contributions, but not the interaction of the tip end with the substrate, which in the case of a thin film samples is still very relevant. Hence, their use do not eliminates topographic cross-talk effects. Finally, the approach proposed by Farina et al.,<sup>42</sup> based in analysing the SMM response in time rather than in frequency, while allowing to cancel the stray, it doesn't solve the problem of the local signal changes due to the tip vertical movement, which still occurs between the tip apex and the sample. In this scope, our method represents a valid option to resolve these issues, which is even applicable with non-optimal conventional, and widely available, conductive AFM probes.

## Experimental

**Atomic Force Microscopy and Scanning Microwave Microscopy Imaging.** The AFM-SMM used in this work has been described thoroughly in former works.<sup>24,35</sup> Briefly, it consists of a Keysight 5600

AFM system in which a conductive tip is connected to a microwave source/meter (a Keysight E8362B vector network analyser, VNA), through a transmission line and a matching impedance,  $Z_0$ . While scanning the tip over the sample in conventional AFM imaging modes, the tip also acts as an emitting-receiving nanoantenna, irradiating a signal highly localized at the apex and at a frequency minimizing the reflections. Depending on the local impedance, part of the signal is reflected back travelling from the antenna to the VNA and recorded as a complex scattering parameter,  $S_{11}$ . This signal is converted into capacitance variation and conductance variation using a low frequency electrostatic force curve, previously acquired, following the calibration methodology described elsewhere.<sup>35</sup> With this system, we acquired single point approach curves, contact mode images, and intermittent contact mode images at a frequency of  $\sim 19$  GHz and VNA IF bandwidth of  $\sim 500$  Hz (power = 3 dBm), with a resolution of 256x256 pixels. The calibration EFM force curves were acquired by applying a 3 V voltage at 2 kHz frequency and recording the second harmonic amplitude  $2\omega$ . Solid platinum 25Pt400B AFM tips from Rocky Mountains Nanotechnology (nominal spring constant of  $\sim 18$  N/m) were used. The noise level in the capacitance measurement is about 6aF. Note that the cross-section profiles shown in Figs. 1-4 correspond to the average obtained from 5 consecutive lines in the measured images. The tip apex radius of the tips,  $R$ , and the stray capacitance rate,  $k_{stray}$ , are determined via least square fitting of an experimental single-point approach curves on the bare metal to the theoretical model in Eqs. (1)-(4), with  $h=0$  nm (metal limit), as shown elsewhere.<sup>32,33</sup> The rest of the geometrical parameters is kept fixed to their nominal values: cone height  $H=80$   $\mu\text{m}$  and cone half angle  $\theta=10^\circ$ .

#### Topographic cross-talk removal and intrinsic capacitance images.

Intrinsic capacitance images have been obtained from the measured capacitance images by subtraction of the topographic cross-talk contribution, following the procedure recently presented elsewhere.<sup>24</sup> In a nutshell, a topographic cross-talk capacitance image is reconstructed by assigning at each pixel the capacitance given by a capacitance approach curve acquired on the metallic substrate at the height of the given pixel. Then, this image is subtracted from the measured capacitance image, to give rise to the intrinsic capacitance image. In order to use the same reference capacitance values in both the capacitance images and the capacitance approach curves, the latter are vertically shifted in order to set the capacitance variation at contact with the substrate in the approach curve to the same value obtained from the capacitance image.

**Non-planar thin film sample fabrication.** The samples consisting of  $\text{SiO}_2/\text{Al}_2\text{O}_3$  micropatterned thin film pillars on a gold coated silicon wafer were fabricated as follows. The gold layer was deposited on a silicon wafer by thermal evaporation, using 10 nm Cr as adhesion layer. After photolithography (AZ 1512 HS positive photoresist, Microchemicals) and development of the exposed resist (AZ 726 MIF developer, Microchemicals), about 65 nm (sample 1) and 140 nm (sample 2) of  $\text{SiO}_2$  (Umicore) were deposited by e-beam evaporation.

Subsequently, a lift-off process was performed in order to obtain the corresponding  $\text{SiO}_2$  square structures on the gold coated silicon wafer. Next, a second photolithography, development, e-beam deposition and lift-off process were performed in order to deposit the 104 nm (sample 1) and 130 nm (sample 2) layer of  $\text{Al}_2\text{O}_3$  (Umicore), and micropattern them at about 5 microns apart from the  $\text{SiO}_2$  structures already present on the gold coated silicon wafer. Micropatterned thermal grown  $\text{SiO}_2$  samples on highly doped silicon wafers have been produced by AMO GmbH.

**Numerical simulations.** To determine the effects of the lateral dimensions of the micropatterned oxides on the intrinsic capacitance values, we used a 2D axisymmetric model described thoroughly in a former work, where it was applied to study the finite-size effects of thin dielectric oxides on electrostatic force microscopy measurements.<sup>33</sup> In the present context, instead of capacitance gradient, we calculate the tip-sample capacitance by integration of the surface charge density on the tip. Since the sample is located within the near-field region of the probe, the microwave field distribution is found in a static approximation, i.e. by solving Poisson's equation. In the geometrical model, the tip is represented by a truncated cone ending with a hemisphere. Since, the intrinsic capacitance image does not contain any stray contribution, it is possible to omit the geometrical parts representing the cantilever and other microscopic components responsible of long range interactions.

## Conclusions

We presented a method that enables mapping the GHz electric permittivity properties of non-planar thin film heterogeneous samples from AFM-SMM capacitance images acquired in contact mode. We showed that by constructing an intrinsic capacitance image, in which topographic cross-talk contributions are subtracted, one can derive directly a local electric permittivity image of the sample with just knowledge of the tip radius, and no effect of the material thickness. In addition, we have shown that for samples containing a reference material with known electric permittivity properties, the derivation of the quantitative electric permittivity map can be obtained even without knowing any information regarding the tip geometry. In the derivation of these results, it is key the use of contact mode imaging. In the case of non-contact imaging modes (such as intermittent contact mode, constant height or two pass modes very often used in SMM measurements) the interpretation of the intrinsic capacitance images in terms of the materials electric permittivity is not direct, since they are still affected by the thickness of the sample. Present findings represent a crucial step towards a quick and straightforward quantification of the electric microwave properties of 3D heterogeneous samples, and we believe that they can facilitate the way to the still rather unexplored field of microwave electrical characterization of three-dimensional structures.

## Acknowledgements

This work has been partially supported by the Nanomicrowave project funded from the European Union Seventh Framework Programme (FP7/People-2012-ITN) under grant agreement n° 317116.EU, and also by the Spanish project TEC2013-48344-C2. (GG) acknowledges support from an ICREA Academia grant from the Generalitat de Catalunya. We acknowledge F. Kienberger from Keysight Technologies for discussions on the results of the work, R. Lazaro from IBEC for useful discussions on the numerical calculations, and M. Cazorla and M. Pla, from the Nanotechnology Platform from IBEC, for the fabrication of the oxide samples.

## References

- 1 E. A. Ash and G. Nicholls, *Nature*, 1972, **237**, 510.
- 2 V. V. Talanov, A. Scherz, R. L. Moreland, and A. R. Schwartz, *Appl. Phys. Lett.*, 2006, **88**, 192906.
- 3 D. E. Steinhauer, C. P. Vlahacos, F. C. Wellstood, S. M. Anlage, C. Canedy, R. Ramesh, A. Stanishevsky, and J. Melngailis, *Rev. Sci. Instrum.*, 2000, **2751**, 12.
- 4 U. Dürig, D. W. Pohl, and F. Rohner, *J. Appl. Phys.*, 1986, **59**, 3318.
- 5 K. Lai, W. Kundhikanjana, H. Peng, Y. Cui, M. A. Kelly, and Z. X. Shen, *Rev. Sci. Instrum.*, 2009, **80**, 2007.
- 6 K. Lai, W. Kundhikanjana, M. A. Kelly, and Z.-X. Shen, *Appl. Nanosci.*, 2011, **1**, 13.
- 7 K. Lai, M. B. Ji, N. Leindecker, M. A. Kelly, and Z. X. Shen, *Rev. Sci. Instrum.*, 2007, **78**, 063702.
- 8 Y. Yang, K. Lai, Q. Tang, W. Kundhikanjana, M. A. Kelly, K. Zhang, Z. Shen, and X. Li, 2012, *J. Micromech. Microeng.*, **22**, 115040.
- 9 U. Kaatze, *Meas. Sci. Technol.*, 2013, **24**, 012005.
- 10 C. Gao, B. Hu, I. Takeuchi, K.-S. Chang, X.-D. Xiang, and G. Wang, *Meas. Sci. Technol.*, 2004, **16**, 248.
- 11 H. Chang, I. Takeuchi, and X. D. Xiang, *Appl. Phys. Lett.*, 1999, **74**, 1165.
- 12 H. Chang, C. Gao, I. Takeuchi, Y. Yoo, J. Wang, P. G. Schultz, and X. Xiang, *Appl. Phys. Lett.*, 1998, **72**, 2185.
- 13 B. Wen, X. X. Wang, W. Q. Cao, H. L. Shi, M. M. Lu, G. Wang, H. B. Jin, W. Z. Wang, J. Yuan, and M. S. Cao, *Nanoscale*, 2014, **6**, 5754.
- 14 J. Liu, W.-Q. Cao, H.-B. Jin, J. Yuan, D.-Q. Zhang, and M.-S. Cao, *J. Mater. Chem. C*, 2015, **3**, 4670.
- 15 K. Lai, M. Nakamura, W. Kundhikanjana, M. Kawasaki, Y. Tokura, M. A. Kelly, and Z.-X. Shen, *Science*, 2010, **329**, 190–119.
- 16 V. V. Talanov, C. Del Barga, L. Wickey, I. Kalichava, E. Gonzales, E. A. Shaner, A. V. Gin, and N. G. Kalugin, *ACS Nano*, 2010, **4**, 3831.
- 17 W. Kundhikanjana, K. Lai, H. Wang, H. Dai, M. A. Kelly, and Z. Shen, *Nano Lett.*, 2009, **9**, 3762.
- 18 E. Seabron, S. MacLaren, X. Xie, S. V. Rotkin, J. A. Rogers, and W. L. Wilson, *ACS Nano* 2016, **10**, 360.
- 19 E. Brinciotti, G. Gramse, S. Hommel, T. Schweinboeck, A. Altes, M. a. Fenner, J. Smoliner, M. Kasper, G. Badino, S.-S. Tuca, and F. Kienberger, *Nanoscale*, 2015, **7**, 14715.
- 20 T. Tai, B. G. Ghamsari, T. R. Bieler, T. Tan, and S. M. Anlage, *Appl. Phys. Lett.* 2014, **104**, 232603.
- 21 A. El Fellahi, K. Haddadi, J. Marzouk, S. Arscott, C. Boyaval, T. Lasri, and G. Dambrine, *Conference Record - IEEE Instrumentation and Measurement Technology Conference*, 2015, 1960.
- 22 K. Lai, W. Kundhikanjana, H. Peng, Y. Cui, M. a Kelly, and Z. X. Shen, *Rev. Sci. Instrum.*, 2009, **80**, 043707.
- 23 A. Karbassi, D. Ruf, A. D. Bettermann, C. A. Paulson, D. W. van der Weide, H. Tanbakuchi, and R. Stancliff, 2008, *Rev. Sci. Instrum.*, **79**, 094706.
- 24 M. C. Biagi, R. Fabregas, G. Gramse, M. Van Der Hofstadt, A. Juárez, F. Kienberger, L. Fumagalli, and G. Gomila, *ACS Nano*, 2016, **10** 280–288.
- 25 I. Ferain, C. A. Colinge, and J.-P. Colinge, *Nature*, 2011, **479**, 310.
- 26 J. Kim, A. J. Hong, S. M. Kim, K.-S. Shin, E. B. Song, Y. Hwang, F. Xiu, K. Galatsis, C. O. Chui, R. N. Candler, S. Choi, J.-T. Moon, and K. L. Wang, *Nanotechnology*, 2011, **22**, 254006.
- 27 C. Hu, Z. Mou, G. Lu, N. Chen, Z. Dong, M. Hu, and L. Qu, *Phys. Chem. Chem. Phys.*, 2013, **15**, 13038.
- 28 F. Castles, D. Isakov, A. Lui, Q. Lei, C. E. J. Dancer, Y. Wang, J. M. Janurudin, S. C. Speller, C. R. M. Grovenor, and P. S. Grant, *Sci. Rep.*, 2016, **6**, 22714.
- 29 S. Baskaran, J. Liu, K. Domansky, N. Kohler, X. Li, C. Coyle, G. E. Fryxell, S. Thevuthasan, and R. E. Williford, *Adv. Mater.*, 2000, **12**, 291.
- 30 B. Wood, B. McDougall, O. Chan, A. Dent, C.-N. Ni, R. Hung, H. Chen, P. Xu, P. Nguyen, M. Okazaki, D. Mao, X. Xu, R. Ramiraz, M.-P. Cai, M. Jin, W. Lee, A. Noori, M. Shek, and C.-P. Chang, *ECS Trans.*, 2011, **35**, 69.
- 31 A. Tselev, J. Velmurugan, A. V. Ievlev, S. V. Kalinin, and A. Kolmakov, *ACS Nano*, 2016, **10**, 3562.
- 32 L. Fumagalli, G. Ferrari, M. Sampietro, and G. Gomila, *Appl. Phys. Lett.*, 2007, **91**, 243110.
- 33 G. Gomila, G. Gramse, and L. Fumagalli, *Nanotechnology*, 2014, **25**, 255702.
- 34 G. Gomila, J. Toset, and L. Fumagalli, *J. Appl. Phys.*, 2008, **104**, 024315.
- 35 G. Gramse, M. Kasper, L. Fumagalli, G. Gomila, P. Hinterdorfer, and F. Kienberger, *Nanotechnology*, 2014, **25**, 145703.
- 36 T. I. K. Richard S. Muller, *Device Electronics for Integrated Circuits*, 3rd ed. Wiley, 2003.
- 37 K. W. Vogt, M. Houston, M. F. Ceiler, C. E. Roberts, and P. A. Kohl, *J. Electron. Mater.*, 1995, **24**, 751.
- 38 M. F. Ceiler Jr., P. A. Kohl, and S. A. Bidstrup, *J. Electrochem. Soc.*, 1995, **142**, 2067.
- 39 B. Fowler, E. O'Brien, *J. Vac. Sci. Technol. B*, 1994, **12**, 441.
- 40 L. Fumagalli, G. Ferrari, M. Sampietro, and G. Gomila, *Nano Lett.*, 2009, **9**, 1604.
- 41 G. Gramse, E. Brinciotti, A. Lucibello, S. B. Patil, M. Kasper, C. Rankl, R. Giridharagopal, P. Hinterdorfer, R. Marcelli, and F. Kienberger, *Nanotechnology*, 2015, **26**, 135701.
- 42 M. Farina, A. Lucasoli, T. Pietrangelo, A. di Donato, S. Fabiani, G. Venanzoni, D. Mencarelli, T. Rozzi, and A. Morini, *Nanoscale*, 2011, **3**, 3589.